Homo-Site Nucleation Growth of Twisted Bilayer MoS$_2$ with Commensurate Angles

Jun Zhou, Haojie Huang, Zihan Zhao, Zhenglong Dou, Li Zhou, Tiantian Zhang, Zhiheng Huang, Yibiao Feng, Dongxia Shi, Nan Liu, Jian Yang, J.C. Nie, Ququan Wang, Jichen Dong,* Yunqi Liu, Ruifen Dou,* and Qikun Xue*

Moiré superlattices, composed of two layers of transition metal dichalcogenides with a relative twist angle, provide a novel platform for exploring the correlated electronic phases and excitonic physics. Here, a gas-flow perturbation chemical vapor deposition (CVD) approach is demonstrated to directly grow MoS$_2$ bilayer with versatile twist angles. It is found that the formation of twisted bilayer MoS$_2$ homostructures sensitively depends on the gas-flow perturbation modes, correspondingly featuring the nucleation sites of the second layer at the same (homo-site) as or at the different (hetero-site) from that of the first layer. The commensurate twist angle of ≈22° in homo-site nucleation strategy accounts for ≈16% among the broad range of twist angles due to its low formation energy, which is in consistence with the theoretical calculation. More importantly, moiré interlayer excitons with the enhanced photoluminescence (PL) intensity and the prolonged lifetime are evidenced in the twisted bilayer MoS$_2$ with a commensurate angle of 22°, which is owing to the reason that the strong moiré potential facilitates the interlayer excitons to be trapped in the moiré superlattices. The work provides a feasible route to controllably built twisted MoS$_2$ homostructures with strong moiré potential to investigate the correlated physics in twistronics systems.

1. Introduction

Since the discovery of Mott insulating states and unconventional superconductivity in magic-angle bilayer graphene,[1,2] the interlayer twist angle has been a new degree of freedom for tuning the energy band structure and exotic electron correlated phenomena due to the confinement of electrons in the moiré superlattices of twisted layered materials. Analogous to graphene-based twisted bilayers, moiré superlattices composed of transition metal dichalcogenide (TMD) materials exhibit novel physical phenomena, such as Mott insulating states,[3–6] Wigner crystal states,[7–9] and quantum anomalous Hall effect.[10] More significantly, plenty of research studies show that moiré excitons are generated in TMD-based twisted heterobilayers of MoSe$_2$/WSe$_2$,[11–14] WSe$_2$/WS$_2$[15] and MoSe$_2$/WS$_2$,[16,17] which originates from the effect of moiré superlattice on interlayer excitons with electrons and holes

J. Zhou, T. Zhang, Y. Feng, J. Yang, J. Nie, R. Dou
School of Physics and Astronomy
Beijing Normal University
Beijing 100875, P. R. China
E-mail: rfdou@bnu.edu.cn

H. Huang, J. Dong, Y. Liu
Beijing National Laboratory for Molecular Sciences
Key Laboratory of Organic Solids
Institute of Chemistry
Chinese Academy of Sciences
Beijing 100190, P. R. China
E-mail: dongjichen@iccas.ac.cn

Z. Zhao, N. Liu
Beijing Key Laboratory of Energy Conversion and Storage Materials
College of Chemistry
Beijing Normal University
Beijing 100875, P. R. China

Z. Dou, L. Zhou
Key Laboratory of Artificial Micro- and Nano-Structures of the Ministry of Education
Hubei Nuclear Solid Physics Key Laboratory
School of Physics and Technology
Wuhan University
Wuhan 430072, P. R. China

Z. Huang, D. Shi
Beijing National Laboratory for Condensed Matter Physics
Institute of Physics
Chinese Academy of Sciences
Beijing 100190, P. R. China

Q. Wang, Q. Xue
Department of Physics
Southern University of Science and Technology
Shenzhen 518055, P. R. China
E-mail: xueqk@sustech.edu.cn

**ADVANCED
SCIENCE NEWS**

www.advancedsciencenews.com

**ADVANCED
MATERIALS**

www.advmat.de

residing in different layers with the type-II band alignment.[18–20] Very recently, it was reported that interlayer excitons can be trapped in the moiré superlattice of twisted MoS_2 homobilayer with a commensurate twist angle of 21.8°.[21] The commensurate angles are theoretically predicted to some "magic" angles in TMD-based homobilayer, with which the twisted homobilayer (THB) structures are explored for the ultra-flat bands and corresponding correlated electron states.[22] This means that the TMD-based THB structures with commensurate angles provide a new platform to engineer the energy band structures and many-body properties of excitons. However, to date, there is still less contribution deliberated to the study of twist angle dependent moiré excitons in TMD-based THB. Therefore, the fabrication of TMD-based THB is a prerequisite for a deep understanding of the twist angle driving the moiré effect on the interlayer excitons (IE).

For the controllable fabrication of twisted layered materials, much efforts have been made to develop different routes including transfer methods, for example, polymer-based dry transfer or liquid-assisted wet transfer,[23–25] folding methods,[26] as well as chemical vapor deposition (CVD) methods.[27–29] The shortcoming of the transfer and folding approaches is the introduction of the interfacial contamination, defects, wrinkles, and bubbles, which greatly inhibit the performances of twisted layered materials utilized in the real twistronic nanodevices. As for the CVD method, it is a well-accepted feasible, and easy approach to acquire high-quality large scale 2D materials.[28,29] However, the direct growth of the TMD-based THB architectures with controllable twist angles by using the CVD method still remains less reported. Therefore, it is necessary to develop a universal CVD approach to directly grow twisted TMD homobilayers and further understand the growth mechanism behind this universal growth way, which may provide a feasible route to engineer the impact of the twist-angle-dependent moiré superlattice on the energy band structures and moiré potential trapped excitons in the TMD-based THB structures.

Here, a universal CVD growth approach is designed to successfully build MoS_2 bilayer homostructures with versatile twist angles ranging from 8° to 56° by using the gas-flow perturbation mode. This method enables the nucleation site of the second layer to be the same (the homo-site nucleation) or different (the hetero-site nucleation) from that of the first layer, which correspondingly depends on the different growth processes mainly including the continuous variation of the gas flow and the discontinuous variation of the gas flow. Through counting the distribution of twist angles of over 2000 twisted MoS_2 bilayer patterns grown by the homo-site nucleation mode, we find that the fraction of the commensurate twist angle near to ≈22° (and ≈32°) accounts for nearly 16%, except that the distribution of the twist angle of 30° is the highest approaching to about 9% of the total angle population. The higher formation probability of commensurate twist angles is mainly driven by the lower formation energy of the THB MoS_2, as intensively illustrated by our theoretical simulation. Moreover, we find that the distribution of twist angles obeys the normal distribution under the continuous growth mode.

Additionally, low temperature (LT) photoluminescence (PL) results demonstrate that the PL intensity of interlayer excitons is prominently enhanced and the peak position of interlayer excitons strongly depends on the PL excitation power in the twisted homobilayer MoS_2 at the commensurate twist of ≈22° (≈32°), compared to that of the THB structures at incommensurate angles. This verifies the formation of moiré excitons originating from interlayer excitons trapped by the deep moiré potential resulting from a commensurate angle between two neighboring layers. Compared to the radiative combination lifetime (≈200 ps) of the interlayer excitons in bilayer MoS_2 at incommensurate angels, the lifetime of the trapped moiré interlayer excitons is prolonged significantly up to ≈520 ps for the as-grown bilayer MoS_2 structure with a twist of ≈22°, further suggesting that the origin of moiré excitons comes from the interlayer excitons. Our work provides a feasible method to build the twisted layered materials, which holds the clean and stable interface to scalably explore exotic quantum phenomena and potentially enable the development of quantum computing and quantum information science.

2. Results

2.1. The Homo-Site and Hetero-Site Nucleation Growth Mode

For the bilayer TMD materials, AA and AB stacked patterns are easily prepared during the CVD growth process due to their lowest formation energy.[29] Accordingly, changing the growth microenvironment through the introduction of the gas-flow perturbation to break the growth equilibrium state might be a feasible experimental method to prepare the desirable twisted TMD bilayer structures due to overcoming a higher formation energy barrier.[30] In our experiments, the Ar gas flow is exclusively set as a changeable value during the overall CVD growth process. Other growth parameters such as the substrate temperature and the growth interval are shown in detail in the Methods section. The CVD setup used to fabricate the THB MoS_2 structures is schematically displayed in Figure S1 (Supporting Information). The top-colored polyline in **Figure 1a** shows the gas-flow fluctuating with the growth interval. In our experiment, the whole process during the CVD growth of the MoS_2 crystal can be divided into three stages: the initial stage (**I**) (0–3 min) associating with the substrate temperature increased up from room temperature to 800 °C, the nucleation and the growth stage (**II**) (3–7 min), and the coalescence stage (**III**) (7–10 min) with a constant substrate temperature of 800 °C. The initial stage (**I**) is related to pre-nucleation for the growth of MoS_2, which is independent of the variation of the gas flow rate. For the third growth stage (**III**), this process can be called the after-nucleation period. In other words, the as-grown THB MoS_2 grains commence to coalesce, and a multigrain THB MoS_2 structure might be produced. The most significant stage, determinedly affecting the formation of the twist angle between two neighboring layers, is the second growth stage (**II**). During this stage, the carrier gas flow perturbation distinctly influences the nucleation sites of the top layer and the related orientation between the top and the bottom layer. A large number of reproducible experimental results display that the regularly varied gas flow (the top curve of Figure 1a), that is the constant value of the gas flow changed rate (the bottom-colored line of Figure 1a) promotes the appearance of rotation angle between the neighboring layers and the nucleation sites
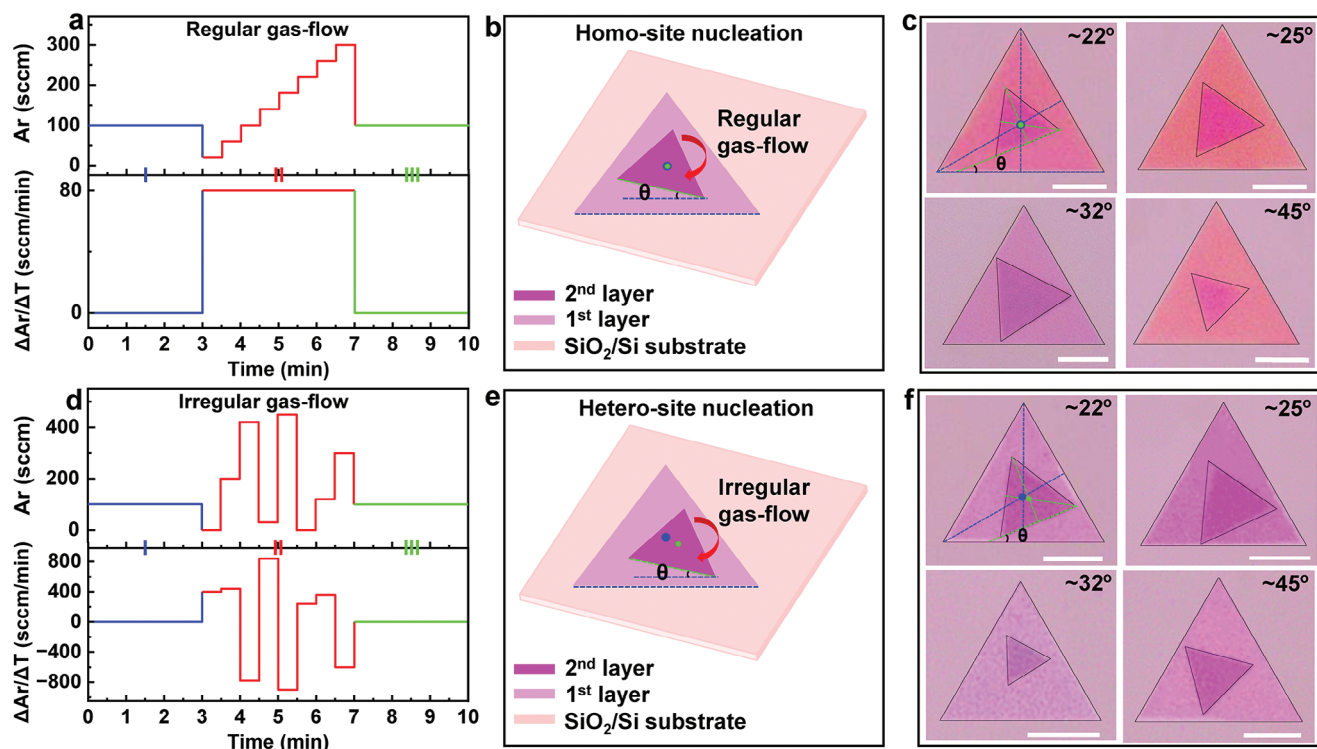
Figure 1. The homo- and hetero-site nucleation strategy for the direct growth of THB MoS₂ structures. a, d) The top image shows the variation in Ar gas flow with the growth interval corresponding to the homo-stie and the hetero-site nucleation growth mode, respectively; the bottom image displays the variation rate of the carrier gas flow with the growth interval, in which the growth interval is divided into three stages: the pre-nucleation stage (**I**) (0–3 min), the nucleation and growth stage (**II**) (3–7 min), and the coalescence stage (**III**) (7–10 min). b, e) A schematic model of the as-grown twisted homobilayer MoS₂ with an interlayer twist, respectively corresponding to the homo- and hetero-site nucleation mode. c,f) Representative OM images of as-grown twisted homobilayer MoS₂ patterns with twist angles of ≈ 22°, 25°, 38°, and 45° for the homo-site and the hetero-site nucleation mode, respectively.

of the top MoS₂ layer located at the same nucleation position as that of the bottom layer, which is named as the homo-site nucleation mode. This is easily understood that the sudden change of the gas flow may interrupt the growth of the first layer. Meanwhile, the sharp increase in the gas flow will easily induce the change of the carrier gas flow direction in the micro-area, which generates the growth rotation of the second layer relative to the first layer. This situation is very similar to the previous results on the CVD growth of twisted bilayer MoSe₂ through the reverse-gas flow method to change the direction of the gas flow after completing the growth of the first layer.[31] However, the stable gas-flow rate may hold the same surrounding microscopic environment during the growth of bilayer MoS₂. In this case, the nucleation sites for the bottom and the top layer are located at the same location, which is the same as that of the growth of bilayer TMDs without the Ar flow perturbation.[32] Previous research on the growth mechanism of 2D layered materials structures have proved that the nucleation site is normally located in the symmetric center of the monolayer crystal.[29,32] The schematic structural model of the homo-site nucleation growth of the THB structures is shown in Figure 1b. The interlayer twist between two layers and the same nucleation sites for the top and the bottom layer are highlighted as the **θ** angle and a green dot at the same site, respectively. Because there is a distinct relationship between the shape of monolayer MoS₂ grown by CVD and its crystal orientation, the

interlayer twist (**θ**) is defined according to the relative direction of the top and bottom triangle edges.[30] Figure 1c shows serials of representative optical microscopy (OM) images of THB-MoS₂ with twist angles of around 22°, 25°, 32° and 45° on SiO₂/Si substrate, which are directly fabricated under the growth condition in the gas flow rate shown in Figure 1a. The twist angle (**θ**) between the top and bottom layer can be experimentally measured by the green and blue dashed lines in the upper left corner image in Figure 1a. In our experiments, the deviation of twist angles is normally about ± 0.5°. The green dot located in Figure 1c represents the same nucleation site for the top and bottom layer. According to the symmetric axis of the patterns respectively coming from the top and bottom layers, one can easily discern that the centers of the top and bottom layers of THB MoS₂ in Figure 1c are overlapped at the same site, evidencing the suggested homo-site nucleation growth mode.

In our experiments, the interlayer twist can be tuned by irregularly manipulating the variation of the Ar gas flow. The top and the bottom polyline in Figure 1d respectively show the inhomogeneous variation of the gas flow and the irregular variation rate with the growth interval. Under the above growth condition, we can obtain THB MoS₂ structures at a wide range of twist angles, which are intuitively shown by OM images of Figure 1e. Obviously, the nucleation sites of the top and the bottom are completely diverse due to the allotopic symmetric centers of the

**ADVANCED
SCIENCE NEWS**

www.advancedsciencenews.com

**ADVANCED
MATERIALS**

www.advmat.de

individual top and bottom layer, as indicated by both symmetric centers (the green and the blue dot) obtained from the top and the bottom layer, respectively. This kind of growth process is referred as the hetero-site nucleation mode. The twisted structures fabricated by CVD through the hetero-site nucleation mode are schematically displayed in Figure 1e. The nucleation sites belonging to the top and the bottom layer are marked as a green and a blue sphere in Figure 1e, respectively. In this case, the interlayer twist is still discerned according to the orientation between two triangle edges. The main difference between the irregular and regular change of the gas flow is the nucleation sites of the top and bottom are varied with the irregular change rate of the Ar gas flow (the bottom curve of Figure 1d). This can be interpreted by the unstable surrounding microscopic environment resulting from the irregularly changing gas flow rate during the growth of bilayer MoS_2. A similar phenomenon has been observed in the CVD growth of twisted bilayer graphene with the hetero-nucleation site growth strategy.[30]

To confirm the influence of the gas flow fluctuation on the nucleation site of the top layer and the introduction of the twist angle between neighboring interlayers, similar regular and irregular variations in the gas flow rate are designed intentionally (Figure S2a,b, Supporting Information). The corresponding as-grown THB MoS_2 structures by using the gas flow turbulence are shown in Figure S2c,d (Supporting Information), which respectively reproduce the growth processes of the homo-site and hetero-site nucleation mode. On the contrary, the stable bilayer MoS_2 structures with AA (0°) or AB (60°) stacking configurations are easily generated during the CVD growth of TMD materials with the constant Ar gas flow, as shown in Figure S2e,f (Supporting Information). Meanwhile, a selected-area electron diffraction (SAED) pattern (Figure S2g, Supporting Information) is obtained, corresponding to the OM image of the twisted bilayer MoS_2 with a twist angle of 20.3° (the left top image in Figure S2c, Supporting Information). To intuitively identify stacking configurations and twist angles existing in as-grown THB MoS_2 patterns, aberration-corrected scanning transmission electron microscopy (STEM) images were further obtained in the representative THB MoS_2 structures, as shown in Figure S3a,d,e (Supporting Information). These STEM images combined with corresponding SAED patterns in Figure S3b,f (Supporting Information) and schematic superlattices in Figure S3c,g (Supporting Information) directly show the periodical moiré patterns, corroborating the evidence of twist angles of 13.4° and 26.7° from the representative twisted bilayer patterns, respectively. Accordingly, one conclusion can be made that the regular perturbation of the gas-flow rate during stage **II** helps to directly obtain twisted bilayer MoS_2 at the homo-site nucleation growth mode, while the gas-flow varied irregularly facilitates to grow twisted bilayer MoS_2 based on the hetero-site nucleation mode.

2.2. Growth Mechanism of the THB MoS$_2$ Directly Fabricated by CVD

It is known that the introduction of the gas-flow oscillation during the CVD growth of MoS_2 is a key parameter for engineering the formation of a twist angle between two neighboring layers in bilayer MoS_2. To understand the reason of the formation of twist angles dominantly ranging from 8° to 56°, the twist angles are statistically counted including thousands of twisted bilayer samples. Interestingly, two twist angles of ≈22° and 32° very nearing to the commensurate angle of 21.8° and 32.2° account for about 16% within counted twist angles beyond 1000 for the as-grown twisted bilayer MoS_2 through the homo-site nucleation mode (**Figure 2a**). Except for a 30° twist angle (≈9%), the formation probability of these two commensurate angles is relatively larger compared to other rotation angles. However, this phenomenon is not reproducible in the statistical counted twist angles formed during the hetero-site nucleation growth of THB-MoS_2 (Figure 2b). In the circumstance of the hetero-site nucleation mode, the rotation angle of 30° appears highest frequently among over 2000 samples of twisted bilayer MoS_2 with the discontinuous gas flow. Meanwhile, it is clearly discerned that THB-MoS_2 homostructures with a small twist angle (< 4°) is not easily to directly grow.[21,30] In a word, the statistical results on twist angles in Figure 2a,b) present a normally distributed population, which evidences that twist angles at a wide range of from 16° to 46° can be grown easily by designing the experimental parameters.

Density function theory (DFT) calculations were performed to understand the above experimental phenomenon. Figure 2c shows the interlayer binding energy profile of a commensurate THB MoS_2 supercell as a function of its interlayer twist angle (Figure S4, Supporting Information). It can be seen that the strongest binding energies correspond to the 3R and 2H crystal structure with a rotation angle of 0° and 60°, respectively. Hence, the 3R and 2H stacking MoS_2 structure are preferential to form during the growth of the MoS_2 bulk material. However, no obvious preference is observed for other twist angles. Previous studies have shown that the orientation of a 2D crystal grown on a substrate is determined at its nucleation stage, where the interaction between the edges of the 2D crystal and the substrate plays a dominant role.[33] To reveal this effect, the relative stabilities of a small triangular MoS_2 island on a perfect MoS_2 surface with different twist angles are calculated (Figure 2d; Figure S5, Supporting Information). It is found that the structure with a twist angle smaller than 18° or larger than 42° is unstable and spontaneously optimized to the structure with 0° or 60° twist angle, consistent with our experimental observation that structures with too small or too large twist angles are scarce. We further testified this point by optimizing a larger triangular MoS_2 island on a MoS_2 surface with a twist angle of 10°, which also spontaneously rotates to 0° (Figure 2e,f). More importantly, local minima are found in the relative energy profile for the twisted angles ranging from 20° to 32° (Figure 2d), which may be corresponding to special commensurate angles including 22° and 32° observed in our experiments. It is noted that the above DFT calculations provide thermodynamic insights into the twist angle distribution in THB MoS_2. To realize the growth of bilayer MoS_2 islands with a relatively large proportion of moiré superlattices, the introduction of a kinetic factor, i.e., the gas flow perturbation, is indispensable. During the CVD growth of MoS_2 layered structure, after the nucleation of the first MoS_2 layer, a sudden increase of Ar is introduced as a gas-flow perturbation, which would provide more active molybdenum and active sulfur species to fuel the nucleation of the second layer so as to promote the growth

**ADVANCED
SCIENCE NEWS**

www.advancedsciencenews.com

**ADVANCED
MATERIALS**

www.advmat.de
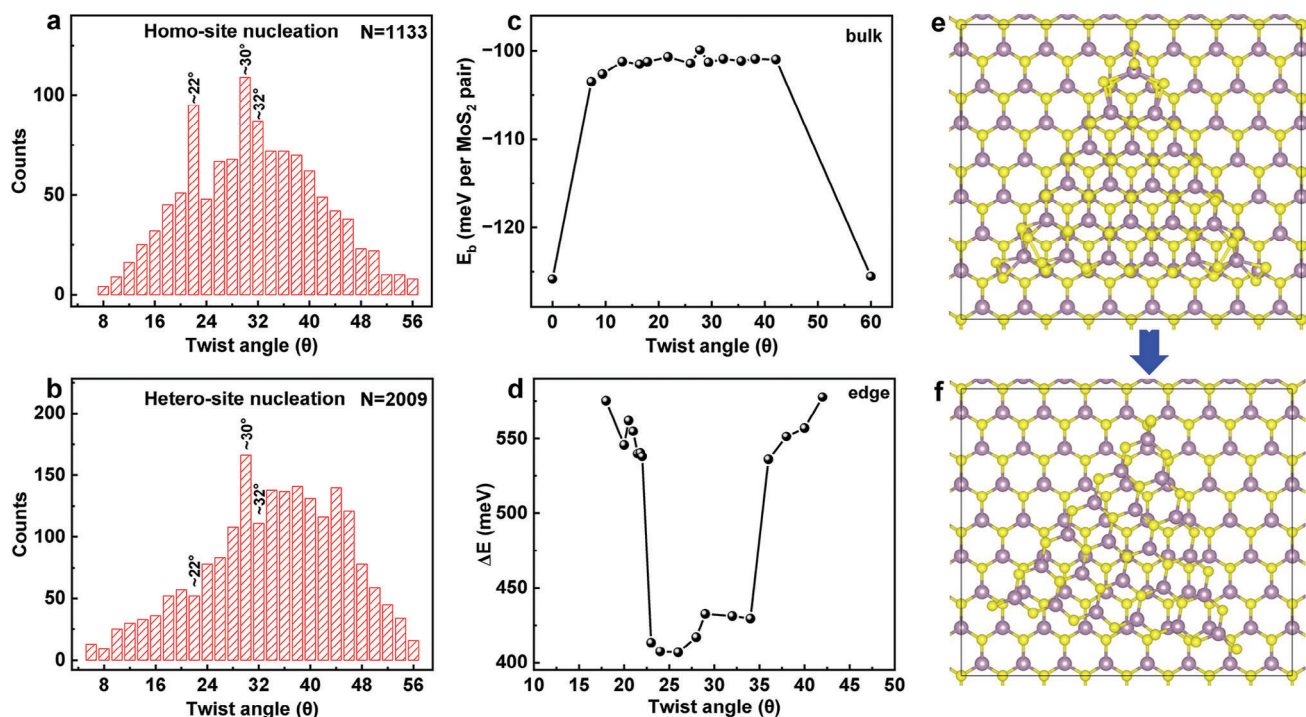
Figure 2. The statistical distribution of twist angles and theoretical calculation of the formation energy for THB MoS$_2$. a, b) The statistic distribution of a wide range of twist angles for the as-grown THB MoS$_2$ grown through the homo-site and the hetero-site nucleation mode, respectively. c,d) The binding energy profile (c) of the THB MoS$_2$ with different twist angles for the bulk and the relative energy profile (d) of a small triangular MoS$_2$ island on MoS$_2$ surface with different twist angles calculated by the DFT. e,f)The atomic structure model of twisted bilayer and zero-twisted bilayer schematically shows that the THB MoS$_2$ can spontaneously reverse back to an energetically stable AA or AB stacked structure with a twist angle of 10°.

of the second MoS$_2$ layer (Figure S6, Supporting Information). A sudden carbon-source supply enhancement is previously reported to be capable of generating new nucleation of the second graphene layer with a rotation angle related to the first layer.[30] In our case, the thermodynamically preferential orientation of the new layer at 0° and 60° would be broken by a different local environment resulting from a sudden increase of the Ar gas flow, enabling the presence of interlayer twist and the formation of THB-MoS$_2$ with a high probability, which is evidenced by the recent report.[34]

2.3. Exploring the Optical Properties of THB MoS$_2$ at Versatile Twist Angles

First, the crystal quality of as-grown THB structures at versatile twist angles was inspected via Raman spectroscopy measurements. **Figures** 3a and S7 (Supporting Information) show representative Raman intensity mapping images of THB MoS$_2$ structures with various twist angles respectively grown through the homo-site and hetero-site nucleation mode (labeled in Figures). The mapping images are obtained by collecting the intensity of
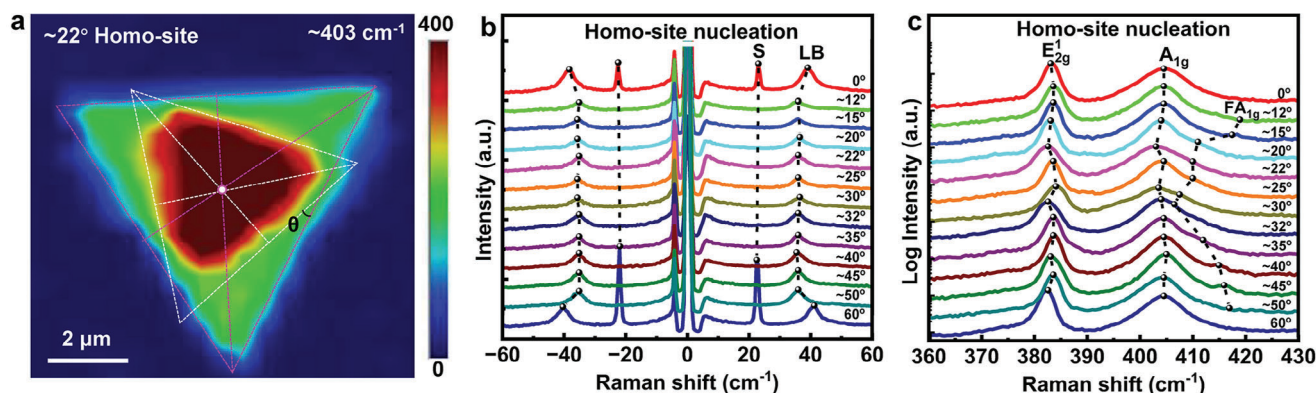
Figure 3. Determination of the twist angles and the interlayer interaction of THB MoS$_2$ at a wide range of twist angles. a) Raman intensity mappings of 22°-THB MoS$_2$ grown through the homo-site nucleation mode, which is obtained through collecting the intensity of the A$_{1g}$ mode. b,c) LF and HF Raman spectra of a series of bilayer MoS$_2$ with different twist angles grown via homo-site nucleation mode.

**ADVANCED
SCIENCE NEWS**

www.advancedsciencenews.com

**ADVANCED
MATERIALS**

www.advmat.de

the A_{1g} modes (the peak energy at ≈404 cm^{-1}). Raman mapping images from Figure 3a and Figure S7a–e (Supporting Information) display the homogenous Raman intensity of A_{1g} vibration in the whole THB MoS$_2$ structures at different twist angles, suggesting that the as-grown.

THB MoS$_2$ possesses a defect-free, uniform, and high-quality crystal structure. The low-frequency (LF) and high-frequency (HF) Raman spectroscopy are universally adopted as a diagnostic tool to characterize the twist angle-dependent interlayer coupling in TMD bilayer.[34–37] The LF and HF Raman spectroscopy measurements of THB MoS$_2$ with different twist angles grown via the homo-site nucleation mode shown in Figure 3b,c further prove that twist angles exist in as-grown THB MoS$_2$ patterns. First, compared with the LF Raman spectrum of bilayer MoS$_2$ with 0° showing a shear (S) mode at 22.87 cm^{-1} and the breath (B) mode at 39.08 cm^{-1}, the S mode is nonexistent and the B mode shifts to the low energy of ≈37.08 cm^{-1} with the introduction of twist angles in THB MoS$_2$. Moreover, the HF Raman spectra in Figure 3c show that FA$_{1g}$ peaks exhibit a sine-like behavior related to twist angles, in agreement with the previous studies on moiré phonon originating from the folded phonon vibration modes.[35–38] These characteristics of the LF and HF Raman spectra provide rational evidence of engineering the interlayer interaction through the introduction of the interlayer rotation angle in 2D layered semiconductor materials, which thus affects their optical and excitonic properties.

It is well-known that in the type-II band aligned stacked TMD heterostructures and the twisted bilayer homostructures, a novel excitonic state of the interlayer exciton can be created,[11–17,21] where the Coulomb coupled electron and the hole are separated between two individual layers as shown in **Figure 4a**. Considering the twisted homobilayer structure, the moiré potential can arise due to different local interactions within the periodical moiré pattern. As shown in Figure 4b, Figures S8 and S9 (Supporting Information), a moiré pattern with a twist angle close to 0° (60°) is composed of high-symmetric AA and 3R (2H, A′B and AB′) regions and transition areas between them. DFT calculations were performed to investigate the electronic band structures and estimate the moiré potential in THB MoS$_2$ (See Supporting Information for calculation details). We found that the variation in direct (indirect) bandgaps between AA and 3R stacking bilayer MoS$_2$ is 78 meV (402 meV), while that between 2H, A′B and AB′ stacking bilayer MoS$_2$ is 37 meV (306 meV). Therefore, the indirect exciton moiré potential depth is much larger than the direct exciton moiré potential depth, and the moiré potential depth for THB MoS$_2$ with a twist angle close to 0° is slightly larger than that with a twist angle close to 60°. Figure 4c,d shows the fitted indirect (Γ-K) and direct (K-K) exciton moiré potentials for a THB MoS$_2$ with a twist angle close to 0°, where the minimum and maximum are located at AA and 3R stacking regions, respectively.[12,21,39] The exact crystalline symmetry, depending sensitively on the fine details of the rotation center, critically affects low-energy response properties.[40] Thus the periodical superlattice causes the electronic dispersion in moiré momentum space and moiré superlattice assists strong interlayer tunneling via Umklapp scattering, which opens new channels for electron kinetics[41] and optical transitions.[42,43] Therefore, moiré superlattice not only provides the deep moiré potential to trap the interlayer excitons and intralayer excitons but also boosts

the super-exchange between them through these high symmetric sites.

In the present experiments, we have measured the optical properties of THB MoS$_2$ structures at different twisted angles by using the PL spectroscopy at room temperature and low temperature (10K). Figure 4e shows the room-temperature (RT) PL spectra of the as-grown THB MoS$_2$ structures at different twist angles of 0°, 22°, 25°, 32° and 45°. One can find that three characteristic peaks from the A exciton (X^A), the B exciton (X^B), and the interlayer exciton exist in the RT PL spectra of THB MoS$_2$. The peaks located at lower energy of 1.4–1.6 eV originating from the emission of the indirect exciton (X^{IE}) strongly depend on twist angles. The peak from the indirect exciton directly indicates the optical bandgap of bilayer MoS$_2$, demonstrating the indirect Γ-K transition in K space corresponding to the top of the valence band and the bottom of the conduction band. Tuned by the twist-dependence interlayer interaction, these optical energy bandgaps upshift with the twist angle varying from 0° to 30° or 60° to 30°. These results are well consistent with our DFT calculations. The calculated direct K-K bandgaps (≈ 2.2 eV) of THB MoS$_2$ show marginal dependence on its twist angle (Figure S8, Supporting Information). Given the exciton binding energy in bilayer MoS$_2$ of 300–400 meV and the spin-orbital coupling effect,[44] the direct K-K bandgaps are responsible for the X^A and X^B excitons. For indirect Γ-K excitons, the most stable 3R (0°) stacking bilayer MoS$_2$ shows a much lower Γ-K bandgap (1.72 eV) than that (2.12 eV) of the meta stable AA stacking structure. With the increase of twist angle from 0°, AA stacking regions appear in THB MoS$_2$ and thus lead to the upshift of indirect bandgaps. Similarly, the most stable 60°-twisted 2H stacking bilayer MoS$_2$ shows a lower Γ-K bandgap (1.821 eV) than that (2.07 eV) of the meta stable A′B stacking structure (Figure S9, Supporting Information). Decreasing the twist angle from 60° would also lead to the increase of Γ-K bandgaps due to the appearance of A′B stacking regions.

Besides, one exciton peak in PL spectra of the bilayer MoS$_2$ with a wide full width at half-maximum (FWHM) means that there may be excitonic complexes except for the natural exciton and the charged exciton. It has been reported that the decrease of temperature leads to crystal lattice contraction[43] and reduced thermal vibrations,[45,46] which contributes to identifying the compositions of many-body exciton complexes. Therefore, different excitonic states including defect excitons (X^D)[47] and moiré exciton (X^{ME})[11–17,21] trapped in the different sites of moiré superlattice related to twisted angles might be detected in low temperature PL spectroscopy.

Figure 4f shows the PL spectra of bilayer MoS$_2$ at rotation angles of 0°, 22°, 25°, 32° and 45°, measured at low temperature of 10K and the laser excitation power of 0.20 mW. Compared to the room-temperature PL spectra (Figure 4e), X^A exciton peaks at approximately 1.90 eV in low-temperature PL spectra of twisted bilayer show a narrow FWHM, almost independent of twisted angles. Moreover, a new characteristic peak is observed on the left side of the X^A exciton peak near 1.78 eV in bilayer and monolayer MoS$_2$. This photon excitation peak can be attributed to the defect-bound local exciton peak (X^D), which is consistent with previous literature reports.[47] The defect exciton state (X^D) usually reflects the crystal quality of the layered MoS$_2$. In our case, the X^D observed in all as-grown samples including bilayer and monolayer MoS$_2$ structures might result from the grain boundary effect due
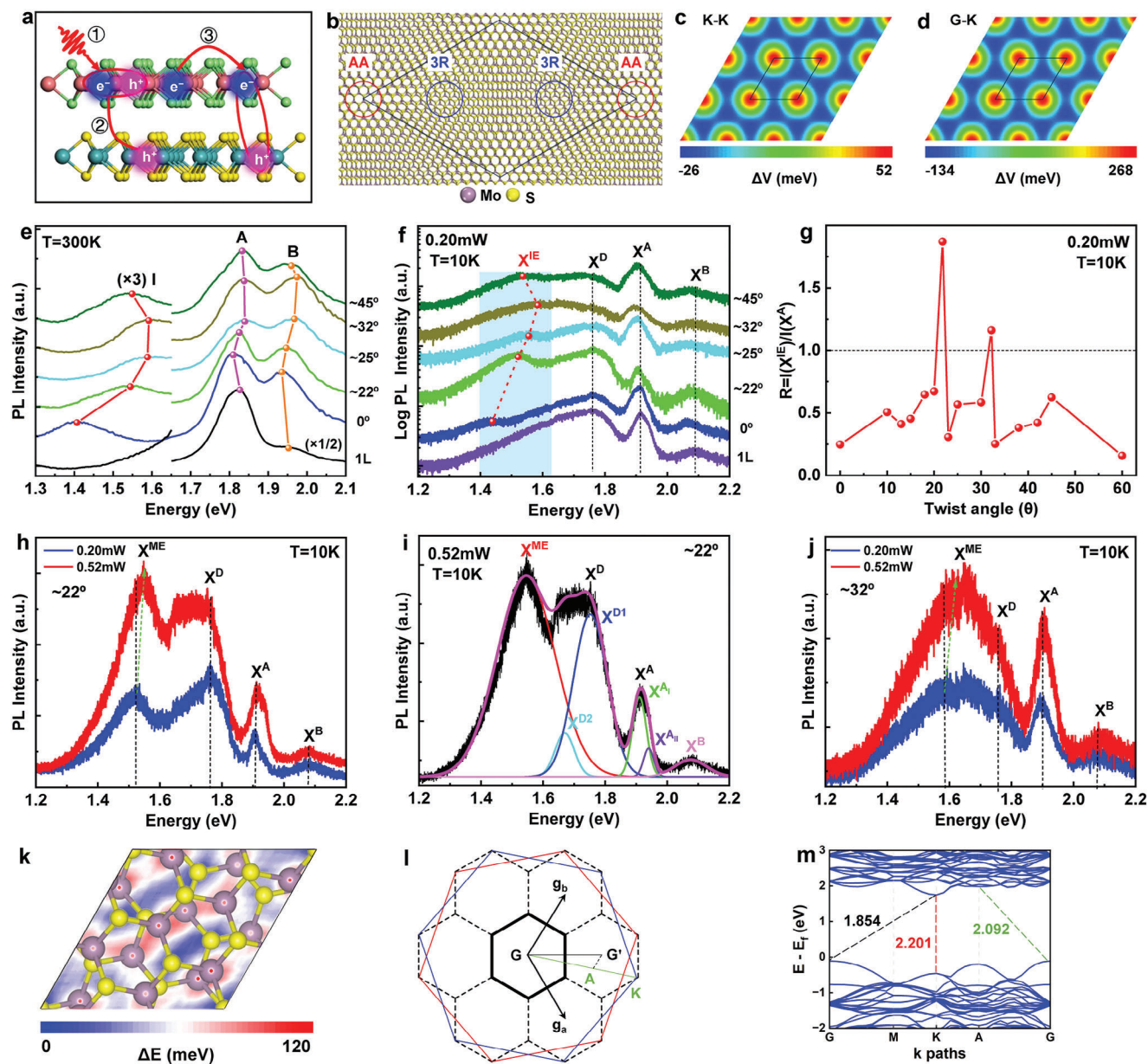
Figure 4. Calculation of the moiré potential and low-temperature (T = 10 K) PL spectra characterization of bilayer MoS_2 with various twist angles. a) Illustration of the light-induced charge separation and the formation of interlayer exciton in the THB-MoS_2 structure. b) Schematic illustration of the moiré superlattice formed in bilayer MoS_2 at a twist angle close to 0° with the moiré unit cell outlined in black. The high symmetric AA and 3R stacking regions are highlighted by red and blue circles, respectively. c,d) Fitted moiré potential for K-K (c) and G-K (d) moiré excitons in HTB MoS_2 with a twist angle close to 0°. e) PL spectroscopy data at room temperature obtained in samples of the MoS_2 monolayer and THB MoS_2 with different twisted angles. f) PL spectroscopy data at low temperature (10K) obtained in samples of the MoS_2 monolayer and THB MoS_2 with different twisted angles. The used laser power is 0.20 mW. g)The intensity ratio of the interlayer excitons (X^{IE}) and the A excitons (X^A) measured from the low temperature PL with a laser power of 0.20 mW. h) PL spectrum at low temperature (10K) of the THB MoS_2 at a twisted angle of 22° with a laser power changing from 0.20 to 0.52 mW. i)The deconvoluted PL curve of the THB MoS_2 at a twisted angle of 22°. j) PL spectrum at low temperature (10K) of the THB MoS_2 at a twisted angle of 32° with a laser power changing from 0.20 to 0.52 mW. k) Average electrostatic potential difference between neutral and positively charged THB MoS_2 at a twisted angle of 22°. l) Brillouin zones of the THB MoS_2 at a twisted angle of 22° (black hexagons) and its component monolayers (red and blue hexagons). m) Electronic band structure of the THB MoS_2 at a twisted angle of 22°. The K path is chosen along the one in (l).

to the multi-step growth of bilayer MoS_2 through the gas-flow perturbation. Meanwhile, a new peak, located at the energy range from 1.50 to 1.62 eV depending on twisted angles, appears on the left side of the X^D peak in the PL spectra of THB MoS_2 at different twisted angles, which still originates from X^{IE} similar to that in PL spectra measured in room temperature. Moreover, the twisted angle has an obvious impact on the intensity of X^{IE}. To understand the twisted angle effect, the intensity ratio of the X^{IE} and the X^A peak of the THB MoS_2 at twisted angles of 0°, 22°, 25°, 32°, and 45° is calculated by the function of $R = I_{X^{IE}}/I_{X^A}$. The relationship of the intensity ratio with the twist angle is displayed in Figure 4g. It is clearly found that the R-value corresponding to the commensurate angle of 22° is the largest, near to 2 among those from THB MoS_2 at twisted angles of 0°, 25°, 32° and 45°. The sharply enhanced PL intensity might be due to the interlayer excitons confined by the deep moiré potential in the different high symmetric sites in moiré superlattices, as shown in Figure 4c,d.[21,48,49] Significantly, the energy value of interlayer exciton trapped by moiré potential is ≈1.54 eV, very close to the previously reported that bilayer MoS_2 at the commensurate twist angle with 21.8° shows an intense moiré exciton peak at 1.60 eV.[21] To ensure the formation of X^{ME}, the low-temperature PL spectroscopy is comparably performed with different laser excitation power of 0.20 and 0.52 mW at an excitation wavelength of 532 nm, as shown in Figure 4h. This clearly shows a blue shift in the energy position of X^{ME} with increasing the laser power, which agrees well with previous results.[11–17,21,22] Meanwhile, the low-temperature PL spectrum of 22°-THB MoS_2 structure with the power of 0.52 mW is fitted by the Gaussian function as shown in Figure 4i, indicating four main peaks, the A exciton (X^A ≈1.92 eV), the B exciton (X^B ≈ 2.03 eV), the defect emission peaks (X^D ≈ 1.74 eV), and the interlayer exciton (X^I ≈1.52 eV), respectively. This further verifies the rational analysis of the many-body exciton complexes. Notably, Figure 4j shows that the laser-power dependent PL spectrum further appears on the sample of 32°-THB MoS_2, demonstrating a blue shift in the energy position of the interlayer exciton with increasing the laser power. However, the PL spectra with changeable laser power performed samples of THB-MoS_2 at incommensurate angles including 0°, 15°, 20°, 24°, 30°, and 60° are shown in Figure S10 (Supporting Information), which have no clues to display the PL spectra influenced by the laser power. Meanwhile, the R-value of 32°-THB MoS_2 is larger than 1 compared to those from THB MoS_2 structures at incommensurate angles (Figure 4g). This means that the intensively enhanced intensity of X^{ME} is strongly related to commensurate twisted angles of 22° and 32° due to the notable effects on optical excitations resulting from a deep moiré potential at the special commensurate angle.[13,21,48,49]

We further calculated the averaged electrostatic potential difference (ΔE) map between the neutral and the positively charged (loss of one electron per unit cell) state of the THB MoS_2 with a commensurate angle of 22° (Figure 4k, See Supporting Information for calculation details), which can provide a quantitative understanding on the distribution of moiré potential at atomic scale. One finds that the variation in ΔE is 120 meV, which is well consistent with our experimentally estimated moiré potential depth. Previous studies have proposed that band folding is also responsible for the strong moiré exciton of THB MoS_2 with a commensurate twist angle.[49,50] Figure 4l,m shows the Brillouin

zone and band structure of the 22°-THB MoS_2. A strong indirect G-A exciton can be found. Therefore, we believe that both the deep moiré potential and band folding contribute to the strong indirect moiré exciton in the THB MoS_2 with a commensurate angle of 22°.
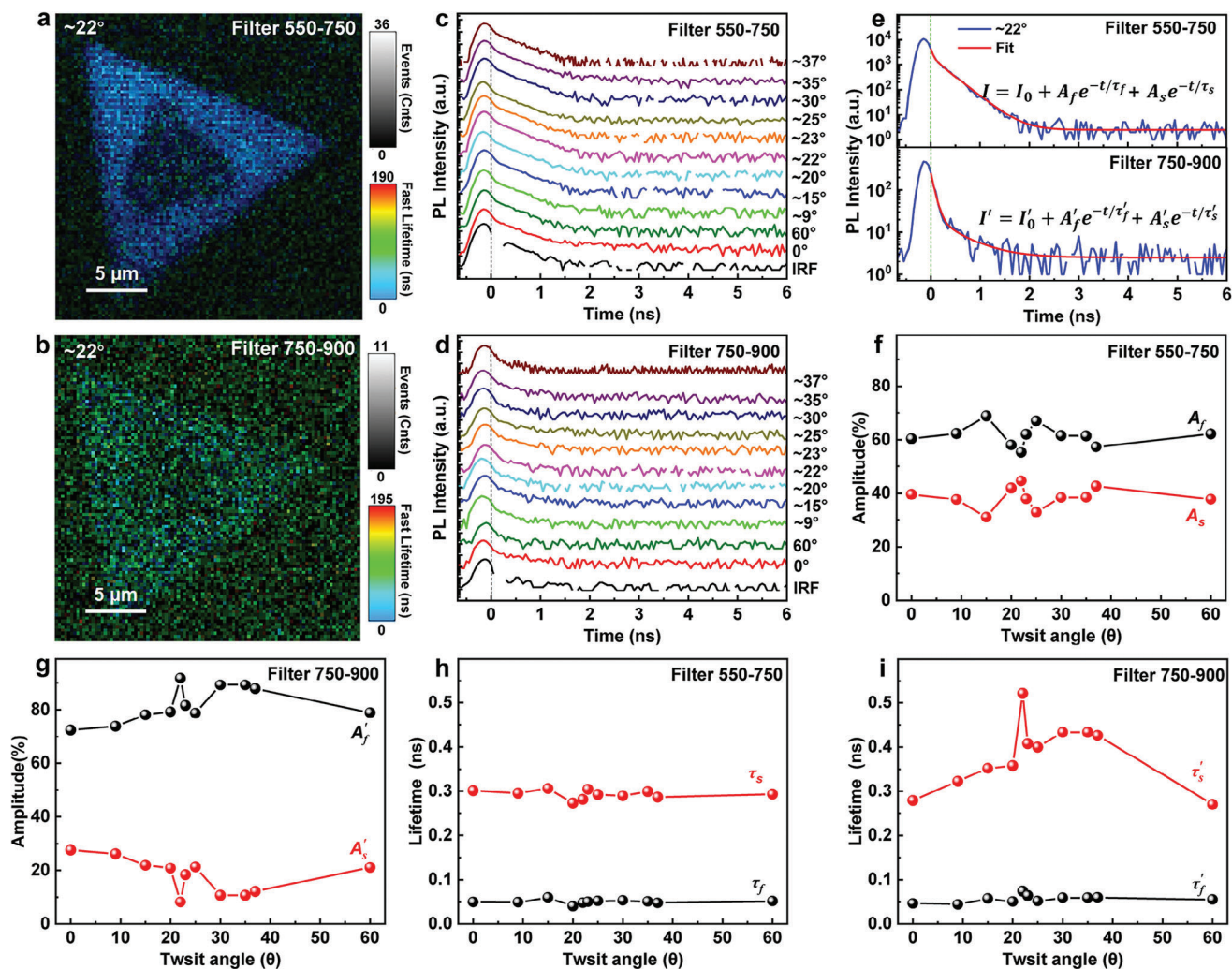
2.4. The Lifetime of Different Exciton Complexes

Recent studies on van der Waals heterostructures have reported the long photoluminescence lifetime and diffusion length of interlayer excitons.[51,52] In the twisted bilayer homostructures and heterostructures at a small or a commensurate twist angle, the twist-angle induced moiré pattern generates a periodic potential landscape that may change the binding energy of the excitons and thus lead to unique photoluminescence lifetimes for the interlayer moiré excitons. The photoluminescent lifetime of interlayer moiré excitons can be experimentally determined using time-resolved (TR) PL spectroscopy. This technique involves probing the dynamics of moiré exciton emission as a function of time, providing access to the exciton lifetime and dynamics. Here, TRPL spectroscopy is comparably carried out in samples of THB MoS_2 structures at a commensurate angle of 22° and varied incommensurate angles (see Figure S11, Supporting Information). **Figure 5a,b** shows TRPL lifetime mapping images of ≈22°-THB MoS_2 structure measured with the emission wavelength filtered by the bandwidth of 550–750 nm and 750–900 nm, respectively. The individual monolayer triangular boundaries in THB MoS_2 at ≈22° can be obviously discerned at the energy range from 1.65 eV to 2.25 eV in Figure 5a, illustrating the strong emission from the direct excitons of X^A. However, the PL from the bilayer region is relatively weak. In contrast, the TRPL lifetime mapping image in Figure 5b mainly displays a resonant emission from the interlayer indirect exciton of X^{IE}, where the bottom monolayer is hard to be identified. Figure 5c,d displays a serial of PL decay curves, respectively corresponding to the X^A and X^{IE} excitons for the THB MoS_2 with varied twist angles. In general, the TRPL decay curve is composed of the fast and slow radiation processes of excitons. To understand the recombination dynamics of the excitons engineered by moiré pattern, the typical TRPL decay curves are fitted by the function of[53]

$$I = I_0 + A_f e^{-t/\tau_f} + A_s e^{-t/\tau_s} \tag{1}$$

which is shown in the top and bottom inset of Figure 5e. Here, I represents the fluorescence intensity decreasing over the measurement time, while I_0 represents the initial fluorescence intensity; τ_f and τ_s is the fast and slow lifetime corresponding to the fast and the slow radiative recombination process, respectively; A_f and A_s is respectively corresponding to the weight of the fast and the slow lifetime, respectively. Accordingly, it was found that the fast lifetime weight (A_f) and slow lifetime weight (A_s) of X^A in the THB-MoS_2 are both maintained ≈60% and 40% respectively, as shown by the black and red curve in Figure 5f, which is consistent with the minimal change in the peak of X^A in room-temperature PL spectrum with respect to the twisted angle. On the contrary, for the interlayer indirect exciton X^{IE}, the fast lifetime weight (A'_f) and slow lifetime weight (A'_s) have an obvious dependence on the twisted angle (Figure 5g), which is related to the sensitivity of

**ADVANCED
SCIENCE NEWS**

www.advancedsciencenews.com

**ADVANCED
MATERIALS**

www.advmat.de

Figure 5. Lifetime of different exciton complexes. a,b) Time-resolved (TR) PL mapping images of 22°-THB MoS$_2$ collected with 550–750 nm (X^A exciton) and 750–900 nm (X^{IE} exciton) bandpass filters, respectively. c,d) TRPL decay curves correspond to the X^A and X^{IE} excitons of THB MoS$_2$ with varied twist angles. e) TRPL curves from ≈22°-THB-MoS$_2$ respectively corresponding to the X^A and X^{IE} excitons, which are fitted by the bi-exponential function. f,g) Lifetime weight coefficients of A_f (A'_f) and A_s (A'_s) resulting from the fast and slow radiative recombination processes of the X^A (X^{IE}) exciton, respectively. h,i)) Lifetime of τ_f (τ'_f) and τ_s (τ'_s) corresponding to the fast and slow radiative recombination processes of the X^A (X^{IE}) exciton, respectively.

the indirect bandgap to the twist angle. Interlayer excitons, corresponding to the indirect excitonic transition from the K to Γ point in the Brillouin zone, involve a recombination process that requires phonon-assisted participation to satisfy the conservation of momentum law. Therefore, the lifetime of the interlayer exciton can be prolonged, which means the longer lifetime of the exciton measured at room temperature may express the recombination dynamics. The red curve in Figure 5h, i respectively shows the slow lifetime of X^{IE} (τ'_s) and X^A (τ_s), suggesting the slow lifetime (τ'_s) of X^{IE} is largest (≈520 ps) at ≈22°-THB-MoS$_2$ structure among as-grown THB MoS$_2$ at an incommensurate angle. This result further verifies that the moiré potential impacts the localization, and the binding energy of interlayer excitons due to the moiré superlattice confinement of interlayer excitons in different superlattice sites. Eventually, the radiative recombination dynamic of the excitons can be engineered through the moiré su-

perlattices of bilayer at a commensurate angle and thus lifetime is lengthened.

3. Conclusion

In summary, a universal CVD growth of twisted bilayer MoS$_2$ with versatile twisted angles is designed. This method enables the direct growth of twisted bilayer through a homo-site nucleation mode or hetero-site nucleation mode, which correspondingly depends on the different growth processes mainly including the continuous variation of the gas flow and the discontinuous variation of the gas flow. The twisted angle distributions are reasonably interpreted by the DFT calculations of the formation energy. Moreover, the moiré excitons are directly measured by using PL spectroscopy at low temperature, which is verified by the lengthening photoluminescent lifetime for the interlayer

excitons from THB MoS$_2$ structure with a commensurate angle and attributed to the deep moiré potential confinement as calculated by the DFT. Exploring moiré excitons in twisted bilayer homostructures at a commensurate angle provides insights into the interplay between the moiré-induced potential, electronic structure, and excitonic behavior, offering opportunities for advancing our understanding of exotic quantum phenomena and potentially enabling the development of next-generation optoelectronic devices.

4. Experimental Section

Sample Fabrication: The twisted homobilayer MoS$_2$ patterns were grown on 300-nm-thick SiO$_2$/Si substrate by CVD. During CVD growth process, MoO$_3$ powder (99.9%, 5 mg, Alfa Aesar) and sulfur (99.95%, 50 mg, Alfa Aesar) were placed in different temperature zones. Meanwhile, the SiO$_2$/Si substrate was upside down placed away from the MoO$_3$ precursor at a distance of 1 cm. Here, the argon gas was used as the carrier gas for the MoS$_2$ crystal whole growth. The furnace temperature was ramped from 27 to 800 °C for 20 min with a continuously or discontinuously changeable gas flow rate. The reaction time was kept for 10 min under atmospheric pressure with the gas-flow perturbation (Figure 2; Figure S3, Supporting Information). The temperature of the MoO$_3$ and S precursor was set at 800 and 130 °C for the reaction time, respectively. After finishing the twisted bilayer MoS$_2$ growth, the CVD system was cooled down to room temperature without any assistance.

Experimental Setup: OM images of tB-MoS$_2$ on SiO$_2$/Si substrates (SiO$_2$ thickness: 300 nm) were obtained by OM (BX51M, Olympus Company).

The room temperature PL spectra were measured with a confocal Raman microscope (InVia, Renishaw U.K.) equipped with 100 lines/mm gratings and × 100 objective lens with a 532 nm He-Cd laser as the excitation source.

The room temperature Raman spectra and low temperature PL spectra were measured at T = 300K and T = 10K using a micro-Raman system (Horiba, LabRAM HR Evolution NANO) equipped with 1800 lines/mm gratings, × 100 objective lens, and 600 lines/mm gratings, × 50 objective lens with laser energy of 2.33 eV (532 nm), respectively.

The time-resolved PL lifetime imaging was measured in a fluorescence lifetime microscope (PicoQuant MicroTime 200) using a pulse laser excitation with a wavelength at 630 nm and a repetition frequency of 5.0 MHz. The emission of direct exciton X^A was collected using a bandpass filter with a bandwidth of 550–750 nm (1.65–2.25 eV), and the emission of interlayer indirect exciton X^{IE} was collected using a bandpass filter with bandwidth of 750–900 nm (1.38–1.65 eV).

Density Functional Theory Calculations: Density functional theory (DFT) calculations were performed by using the Vienna ab initio simulation Package. The detailed calculation methods are provided in Supplementary Materials.

Supporting Information

Supporting Information is available from the Wiley Online Library or from the author.

Conflict of Interest

The authors declare no conflict of interest.

Author Contributions

J.Z. and H.J.H. contributed equally to this work. R.F.D. and J.Z. conceived the present experiments. J.Z. prepared the samples of twisted bilayer MoS$_2$ on SiO$_2$/Si substrates. H.J.H, Y.Q.L., and J.C.D performed the DFT calculation work. J.Z., Z.H.Z., T.T.Z., Y.B.F., J.Y., and N.L. carried out the Raman spectrum measurements. J.Z., Z.H.H, and S.X.D. performed the PL measurements at low temperature. J.Z., Z.L.D., L.Z., Q.Q.W., and Q.K.X. carried out the measurements of the lifetime of the excitons. R.F.D. completed writing the text and discussed it with J.C.N., J.C.D., and Q.K.X. All authors discussed the results and commented on the manuscript.

Data Availability Statement

The data that support the findings of this study are openly available in Homo-Site Nucleation Growth of Twisted Bilayer MoS$_2$ with Commensurate Angles at https://doi.org/10.1002/adma.202408227, reference number 53.

[1] Y. Cao, V. Fatemi, A. Demir, S. Fang, S. L. Tomarken, J. Y. Luo, J. D. Sanchez-Yamagishi, K. Watanabe, T. Taniguchi, E. Kaxiras, R. C. Ashoori, P. Jarillo-Herrero, *Nature* **2018**, *556*, 80.

[2] Y. Cao, V. Fatemi, S. Fang, K. Watanabe, T. Taniguchi, E. Kaxiras, P. Jarillo-Herrero, *Nature* **2018**, *556*, 43.

[3] L. Wang, E. M. Shih, A. Ghiotto, L. Xian, D. A. Rhodes, C. Tan, M. Claassen, D. M. Kennes, Y. S. Bai, B. Kim, K. Watanabe, T. Taniguchi, X. Y. Zhu, J. Hone, A. Rubio, A. N. Pasupathy, C. R. Dean, *Nat. Mater.* **2020**, *19*, 861.

[4] A. Ghiotto, E.-M. Shih, G. S. S. G. Pereira, D. A. Rhodes, B. Kim, J. Zang, A. J. Millis, K. Watanabe, T. Taniguchi, J. C. Hone, L. Wang, C. R. Dean, A. N. Pasupathy, *Nature* **2021**, *597*, 345.

[5] Y. Tang, L. Li, T. Li, Y. Xu, S. Liu, K. Barmak, K. Watanabe, T. Taniguchi, A. H. MacDonald, J. Shan, K. F. Mak, *Nature* **2020**, *579*, 353.

[6] Y. Xu, S. Liu, D. A. Rhodes, K. Watanabe, T. Taniguchi, J. Hone, V. Elser, K. F. Mak, J. Shan, *Nature* **2020**, *587*, 214.

[7] E. C. Regan, D. Wang, C. Jin, M. I. Utama, B. Gao, X. Wei, S. Zhao, W. Zhao, Z. Zhang, K. Yumigeta, M. Blei, J. D. Carlstrom, K. Watanabe, T. Taniguchi, S. Tongay, M. Crommie, A. Zettl, F. Wang, *Nature* **2020**, *579*, 359.

[8] Y. Zhou, J. Sung, E. Brutschea, I. Esterlis, Y. Wang, G. Scuri, R. J. Gelly, H. Heo, T. Taniguchi, K. Watanabe, G. Zarand, M. D. Lukin, P. Kim, E. Demler, H. Park, *Nature* **2021**, *595*, 48.

[9] H. Li, S. Li, E. C. Regan, D. Wang, W. Zhao, S. Kahn, K. Yumigeta, M. Blei, T. Taniguchi, K. Watanabe, S. Tongay, A. Zettl, M. F. Crommie, F. Wang, *Nature* **2021**, *597*, 650.

[10] T. Li, S. Jiang, B. Shen, Y. Zhang, L. Li, Z. Tao, T. Devakul, K. Watanabe, T. Taniguchi, L. Fu, J. Shan, K. F. Mak, *Nature* **2021**, *600*, 641.

[11] T. Kha, G. Moody, F. Wu, X. Lu, J. Choi, K. Kim, A. Rai, D. A. Sanchez, J. Quan, A. Singh, J. Embley, A. Zepeda, M. Campbell, T. Autry, T. Taniguchi, K. Watanabe, N. Lu, S. K. Banerjee, K. L. Silverman, S. Kim, E. Tutuc, L. Yang, A. H. MacDonald, X. Li, *Nature* **2019**, *567*, 71.

[12] K. L. Seyler, P. Rivera, H. Yu, N. P. Wilson, E. L. Ray, D. G. Mandrus, J. Yan, W. Yao, X. Xu, *Nature* **2019**, *567*, 66.

[13] K. Shinokita, Y. Miyauchi, K. Watanabe, T. Taniguchi, K. Matsuda, *Nano Lett.* **2021**, *21*, 5938.

[14] M. Foerg, A. S. Baimuratov, S. Y. Kruchinin, I. A. Vovk, J. Scherzer, J. Foerste, V. Funk, K. Watanabe, T. Taniguchi, A. Hoegele, *Nat. Commun.* **2021**, *12*, 1656.

[15] C. Jin, E. C. Regan, A. Yan, M. I. B. Utama, D. Wang, S. Zhao, Y. Qin, S. Yang, Z. Zheng, S. Shi, K. Watanabe, T. Taniguchi, S. Tongay, A. Zettl, F. Wang, *Nature* **2019**, *567*, 76.

[16] E. M. Alexeev, D. A. Ruiz-Tijerina, M. Danovich, M. J. Hamer, D. J. Terry, P. K. Nayak, S. Ahn, S. Pak, J. Lee, J. I. Sohn, M. R. Molas, M. Koperski, K. Watanabe, T. Taniguchi, K. S. Novoselov, R. V. Gorbachev, H. S. Shin, V. I. Fal'ko, A. I. Tartakovskii, *Nature* **2019**, *567*, 81.

[17] L. Zhang, Z. Zhang, F. Wu, D. Wang, R. Gogna, S. Hou, K. Watanabe, T. Taniguchi, K. Kulkarni, T. Kuo, S. R. Forrest, H. Deng, *Nat. Commun.* **2020**, *11*, 5888.

[18] P. Rivera, H. Yu, K. L. Seyler, N. P. Wilson, W. Yao, X. Xu, *Nat. Nanotech.* **2018**, *13*, 1004.

[19] X. Hong, J. Kim, S.-F. Shi, Y. Zhang, C. Jin, Y. Sun, S. Tongay, J. Wu, Y. Zhang, F. Wang, *Nat. Nanotech.* **2014**, *9*, 682.

[20] Y. Liu, C. Zeng, J. Yu, J. Zhong, B. Li, Z. Zhang, Z. Liu, Z. M. Wang, A. Pan, X. Duan, *Chem. Soc. Rev.* **2021**, *50*, 6401.

[21] X. Zhao, J. Qiao, X. Zhou, H. Chen, J. Y. Tan, H. Yu, S. M. Chan, J. Li, H. Zhang, J. Zhou, J. Dan, Z. Liu, W. Zhou, Z. Liu, B. Peng, L. Deng, S. J. Pennycook, S. Y. Quek, K. P. Loh, *Nano Lett.* **2022**, *22*, 203.

[22] S. Tao, X. Zhang, J. Zhu, P. He, S. A. Yang, Y. Lu, S.-H. Wei, *J. Am. Chem. Soc.* **2022**, *144*, 3949.

[23] F. Pizzocchero, L. Gammelgaard, B. S. Jessen, J. M. Caridad, L. Wang, J. Hone, P. Boggild, T. J. Booth, *Nat. Commun.* **2016**, *7*, 11894.

[24] Y. Huang, Y. H. Pan, R. Yang, L. H. Bao, L. Meng, H. L. Luo, Y. Q. Cai, G. D. Liu, W. J. Zhao, Z. Zhou, L. M. Wu, Z. L. Zhu, M. Huang, L. W. Liu, L. Liu, P. Cheng, K. H. Wu, S. B. Tian, C. Z. Gu, Y. G. Shi, Y. F. Guo, Z. G. Cheng, J. P. Hu, L. Zhao, G. H. Yang, E. Sutter, P. Sutter, Y. L. Wang, W. Ji, X. J. Zhou, et al., *Nat. Commun.* **2020**, *11*, 2453.

[25] H. W. Guo, Z. Hu, Z. B. Liu, J. G. Tian, *Adv. Funct. Mater.* **2021**, *31*, 2007810.

[26] B. Wang, M. Huang, N. Y. Kim, B. V. Cunning, Y. Huang, D. S. Qu, X. J. Chen, S. Jin, M. Biswal, X. Zhang, S. H. Lee, H. Lim, W. J. Yoo, Z. Lee, R. S. Ruoff, *Nano Lett.* **2017**, *17*, 1467.

[27] K. Liu, L. Zhang, T. Cao, C. Jin, D. Qiu, Q. Zhou, A. Zettl, P. Yang, S. G. Louie, F. Wang, *Nat. Commun.* **2014**, *5*, 4966.

[28] G. L. Shao, X. X. Xue, X. Liu, D. L. Zhang, Y. Y. Jin, Y. W. Wu, B. Y. You, Y. C. Lin, S. S. Li, K. Suenaga, X. Wang, A. L. Pan, H. M. Li, J. H. Hong, Y. X. Feng, S. Liu, *Chem. Mater.* **2020**, *32*, 9721.

[29] J. Dong, L. Zhang, F. Ding, *Adv. Mater.* **2019**, *31*, 1801583.

[30] L. Sun, Z. Wang, Y. Wang, L. Zhao, Y. Li, B. Chen, S. Huang, S. Zhang, W. Wang, D. Pei, H. Fang, S. Zhong, H. Liu, J. Zhang, L. Tong, Y. Chen, Z. Li, M. H. Rummeli, K. S. Novoselov, H. Peng, L. Lin, Z. Liu, *Nat. Commun.* **2021**, *12*, 2391.

[31] X. Zhang, H. Nan, S. Xiao, X. Wan, X. Gu, A. Du, Z. Ni, K. Ostrikov, *Nat. Commun.* **2019**, *10*, 598.

[32] L. Liu, T. Li, L. Ma, W. Li, S. Gao, W. Sun, R. Dong, X. Zou, D. Fan, L. Shao, C. Gu, N. Dai, Z. Yu, X. Chen, X. Tu, Y. Nie, P. Wang, J. Wang, Y. Shi, X. Wang, *Nature* **2022**, *605*, 69.

[33] X. Zhang, Z. Xu, L. Hui, J. Xin, F. Ding, *J. Phys. Chem. Lett.* **2012**, *3*, 2822 .

[34] M. Xu, H. Ji, L.u Zheng, W. Li, J. Wang, H. Wang, L. Luo, Q. Lu, X. Gan, Z. Liu, X. Wang, W. Huang, *Nat. Commun.* **2024**, *15*, 562 .

[35] X. Zhang, W. P. Han, J. B. Wu, S. Milana, Y. Lu, Q. Q. Li, A. C. Ferrari, P. H. Tan, *Phys. Rev. B* **2013**, *87*, 115413 .

[36] L. Liang, J. Zhang, B. G. Sumpter, Q.-H. Tan, P.-H. Tan, V. Meunier, *ACS Nano* **2017**, *11*, 11777.

[37] J. Quan, L. Linhart, M.-L. Lin, D. Lee, J. Zhu, C.-Y. Wang, W.-T. Hsu, J. Choi, J. Embley, C. Young, T. Taniguchi, K. Watanabe, C.-K. Shih, K. Lai, A. H. MacDonald, P.-H. Tan, F. Libisch, X. Li, *Nat. Mater.* **2021**, *20*, 1100.

[38] M. L. Lin, Q. H. Tan, J. B. Wu, X. S. Chen, J. H. Wang, Y. H. Pan, X. Zhang, X. Cong, J. Zhang, W. Ji, P. A. Hu, K. H. Liu, P. H. Tan, *ACS Nano* **2018**, *12*, 8770.

[39] M. H. Naik, E. C. Regan, Z. Zhang, Y.-H. Chan, Z. Li, D. Wang, Y. Yoon, C. S. Ong, W. Zhao, S. Zhao, M. I. B. Utama, B. Gao, X. Wei, M. Sayyad, K. Yumigeta, K. Watanabe, T. Taniguchi, S. Tongay, F. H.da Jornada, F. Wang, S. G. Louie, *Nature* **2022**, *609*, 52.

[40] C. Chen, D. W. Zhai, C. Xiao, W. Yao, *Phys. Rev. Res.* **2024**, *6*, L012059.

[41] N. P. Wilson, W. Yao, J. Shan, X. Xu, *Nature* **2021**, *599*, 383.

[42] B. Peng, J. Li, Q. Li, Y. Li, H. Zhu, L. Zhang, X. Wang, L. Bi, H. Lu, J. Xie, L. Deng, Q. Xu, K. Loh, *RSC Adv.* **2017**, *7*, 18366.

[43] D. Kozawa, R. Kumar, A. Carvalho, K. K. Amara, W. Zhao, S. Wang, M. Toh, R. M. Ribeiro, A. H. Castro Neto, K. Matsuda, G. Eda, *Nat. Commun.* **2014**, *5*, 4543.

[44] I. C. Gerber, E. Courtade, S. Shree, C. Robert, T. Taniguchi, K. Watanabe, A. Balocchi, P. Renucci, D. Lagarde, X. Marie, B. Urbaszek, *Phys. Rev. B* **2019**, *99*, 035443.

[45] S. Tongay, J. Zhou, C. Ataca, K. Lo, T. S. Matthews, J. B. Li, J. C. Grossman, J. Q. Wu, *Nano Lett.* **2012**, *12*, 5576.

[46] J. S. Ross, S. F. Wu, H. Y. Yu, N. J. Ghimire, A. M. Jones, G. Aivazian, J. Q. Yan, D. G. Mandrus, D. Xiao, W. Yao, X. D. Xu, *Nat. Commun.* **2013**, *4*, 1474.

[47] Y. Q. Wang, L. J. Deng, Q. L. Wei, Y. Wan, Z. Liu, X. Lu, Y. Li, L. Bi, L. Zhang, H. P. Lu, H. Y. Chen, P. H. Zhou, L. B. Zhang, Y. C. Cheng, X. X. Zhao, Y. Ye, W. Huang, S. J. Pennycook, K. P. Loh, B. Peng, *Nano Lett.* **2020**, *20*, 2129.

[48] H. Zheng, B. Wu, C.-T. Wang, S. Li, J. He, Z. Liu, J.-T. Wang, J.-A. Duan, Y. Liu, *Small* **2023**, *3*, 2207988.

[49] Q. Tan, A. Rasmita, Z. Zhang, K. S. Novoselov, W.-b. Gao, *Phys. Rev. Lett.* **2022**, *129*, 247401.

[50] X. Zhao, J. Qiao, X. Zhou, H. Chen, J. Y. Tan, H. Yu, S. M. Chan, J. Li, H. Zhang, J. Zhou, J. Dan, Z. Liu, W.u Zhou, Z. Liu, B.o Peng, L. Deng, S. J. Pennycook, S. Y. Quek, K. P. Loh, *Nano Lett.* **2022**, *22*, 203.

[51] P. Rivera, J. R. Schaibley, A. M. Jones, J. S. Ross, S. Wu, G. Aivazian, P. Klement, K. Seyler, G. Clark, N. J. Ghimire, J. Yan, D. G. Mandrus, W. Yao, X. Xu, *Nat. Commun.* **2015**, *6*, 6242.

[52] D. Unuchek, A. Ciarrocchi, A. Avsar, K. Watanabe, T. Taniguchi, A. Kis, *Nature* **2018**, *560*, 340.

[53] Y. Liu, X. Hu, T. Wang, D. Liu, *ACS Nano* **2019**, *13*, 14416.